

# The orbital alignment of HD 332231 b

## The warm Saturn HD 332231 b/TOI-1456 b travels on a well-aligned, circular orbit around a bright F8 dwarf

E. Knudstrup<sup>1,2</sup> and S. H. Albrecht<sup>1</sup>

<sup>1</sup> Stellar Astrophysics Centre, Department of Physics and Astronomy, Aarhus University, Ny Munkegade 120, DK-8000 Aarhus C, Denmark

e-mail: emil@phys.au.dk

<sup>2</sup> Nordic Optical Telescope, Rambla José Ana Fernández Pérez 7, E-38711 Breña Baja, Spain

Received September 15, 1996; accepted March 16, 1997

### ABSTRACT

**Context.** Contrary to the orthodox picture of planet formation resulting in a neatly ordered Solar System, exoplanet systems show a large diversity of orbits: short and long periods, circular and eccentric, well- and misaligned, even retrograde orbits. In order to understand this diversity it is essential to probe key orbital parameters. Spin-orbit alignment is such a parameter and can allude to the formation and migration history of the system. However, tidal circularization and alignment might hamper the interpretation of orbital eccentricity and obliquities in the context of planet formation and evolution for planets on orbits with less than about ten days.

**Aims.** Here we aim to measure the projected stellar obliquity in the HD 332231 system in which a warm (period  $\approx 18.7$  days) giant planet orbits a bright F star on a circular orbit.

**Methods.** We observed the system during a transit with the HARPS-N spectrograph and obtained data on the Rossiter-McLaughlin effect. We analyze the spectroscopic transit data together with new TESS photometry employing three different analysis methods.

**Results.** The results from the different approaches are fully consistent. We find a projected obliquity of  $-1 \pm 7^\circ$ , indicating the stellar spin axis to be well-aligned with the orbit of the planet. We furthermore find evidence for Transit Timing Variations suggesting the presence of an additional third body in the system.

**Conclusions.** Together with the low orbital eccentricity the good alignment suggests that this warm giant planet has not undergone high eccentricity migration.

**Key words.** methods: observational – techniques: spectroscopic – techniques: photometric – planets and satellites: dynamical evolution and stability – planet-star interactions

## 1. Introduction

Understanding planet formation is intermittently linked to the understanding of the migratory patterns of giant planets. The formation of so called hot Jupiters (HJ) gas giant planets with orbits of less than some 10 days and warm Jupiters (WJs) found at larger separations with orbital periods between around 10 – 200 days is not well understood (see Dawson & Johnson 2018, for a review). In situ formation appears unlikely, at least for the inner planets. Therefore, orbital migration from their original birth orbits to the orbits we now observe them in appears to be an attractive explanation. However, the exact route(s) for such a migration is as of yet not well known.

The two leading theories for orbital shrinkage are “disk-migration” and “high-eccentricity (high- $e$ ) migration” (Dawson & Johnson 2018). In the scenario of “disk-migration”, angular momentum exchanged between the planet and planetary disk, which leads to an in-spiral of the planet (e.g., Lin et al. 1996; Baruteau et al. 2014). “High- $e$  migration” is the result of interactions between multiple bodies in the planetary system. Here the migration can be caused by scattering, which creates a highly eccentric orbit that is subsequently shrunk through tidal circularization (e.g., Nagasawa et al. 2008; Chatterjee et al. 2008), or by a distant stellar or planetary companion in the system, which

causes secular Kozai Lidov Cycles followed by Tidal Friction (e.g., Wu & Murray 2003; Fabrycky & Tremaine 2007; Naoz 2016). In systems with three or more planets exchange of angular momentum can drive the Jupiter’s orbit to large eccentricities in a process known as secular chaos (e.g., Laskar 2008; Wu & Lithwick 2011; Teyssandier et al. 2019), subsequent tidal orbital shrinking can lead to a close in orbiting giant planet.

In general multi body interactions in “high- $e$  migration” heat the orbit of the planet leading to an elliptical/eccentric and inclined orbit with respect to its original orbital plane. Conversely, “disk-migration” is expected to result in low eccentricity near circular orbits located near the mid-plane of the protoplanetary disk in which the planet has formed. Assuming alignment between the stellar equator and the protoplanetary disk stellar obliquities (the angle between the orbital and stellar angular momenta) can be used next to eccentricity measurements to inform theories about planet formation and evolution.

However, such inference is complicated by a number of factors. It has been found that tidal interactions can significantly alter both the obliquity (Winn et al. 2010; Albrecht et al. 2012a) and the eccentricity (e.g., Husnoo et al. 2012; Bonomo et al. 2017). Furthermore, good alignment between the protoplanetary disk and stellar equator is not guaranteed, despite the fact

that the former inherits its angular momentum from the latter. Chaotic accretion might lead to a misaligned stellar and protoplanetary disk spin (Bate et al. 2010; Thies et al. 2011; Fielding et al. 2015; Bate 2018), but see also Takaishi et al. (2020) suggesting only moderate misalignment can be created that way. Magnetic torques might also lead to misalignment (Foucart & Lai 2011; Lai et al. 2011; Romanova et al. 2021). Inclined stellar or planetary companions might tilt disks (see, e.g., Borderies et al. 1984; Lubow & Ogilvie 2000; Batygin 2012; Spalding et al. 2014; Matsakos & Königl 2017). Although Zanazzi & Lai (2018) found that HJs suppress such a misalignment. While most systems observed so far suggest good primordial alignment (Albrecht et al. 2013) at least one system appears to have had a retrograde spinning protoplanetary disk (Hjorth et al. 2021). Finally, orbits might have large inclinations relative to the stellar spin, but this is the result of precession caused by a giant orbiting planetary companion on a wide orbit (Huber et al. 2013; Gratia & Fabrycky 2017).

One class of systems suited to probe evolution pathways of giant planets are WJs, since tides might not have altered the obliquity nor completely dampened the eccentricity. Depending on the presence or absence of a nearby stellar or planetary companion a number of formation and evolution processes may be excluded or considered.

HD 332231 is one such system. It was first detected by the Transiting Exoplanet Survey Satellite (TESS; Ricker et al. 2015) and it was given the ID TOI-1456 (TOI: TESS Object of Interest). It was subsequently confirmed and characterised by Dalba et al. (2020) through radial velocity (RV) measurements. With an orbital period of  $\sim 18.7$  d it was determined to be a warm Jupiter, with a radius slightly larger than Saturn ( $R_p \sim 0.87 R_{\text{Jupiter}}$ ), but with a significantly lower mass ( $M_p \sim 0.24 M_{\text{Jupiter}}$ ). Key parameters for the HD 332231 system is summarized in Table 1.

Here we want to gain information on the obliquity of the host star to further investigate its history. We observed the system with a high resolution spectrograph while the planet was transiting its host. Analysis of the Rossiter-McLaughlin (RM; Rossiter 1924; McLaughlin 1924; Struve & Elvey 1931) effect, a line shape distortion occurring during transits, allows us to determine  $\lambda$ , the sky projection of the stellar obliquity,  $\psi$ .

We describe our observations in Section 2. In Section 3 we use three approaches to determine the projected obliquities from the obtained data sets. After describing our main results in Section 4, we briefly discuss them in context of measurements in similar systems in Section 5 before concluding.

## 2. Observations

HD 332231 was observed by TESS in Sector 14 and 15 with a single transit in both sectors. An additional transit occurred in the observational gap between these two sectors. As noted in Dalba et al. (2020) the transit in Sector 14 was heavily affected by scattered light and was masked out by the presearch data conditioning (PDC) module in the Science Processing Operations Center (SPOC; Jenkins et al. 2016). We initially include all data and correct for this extra background using the RegressionCorrector implemented in *lightcurve* (Lightcurve Collaboration et al. 2018). The background corrected and normalised light curve is shown in Fig. 1. HD 332231 was observed again in the extended mission of TESS in Sector 41 with two consecutive transits. This allows for an improved determination of the ephemeris as well as other photometric transit parameters, especially as the scatter in the Sector 41 lightcurve is significantly lower than in Sector 14 and 15 as seen in Fig. 1.

**Table 1.** Parameters of the HD 332231 system.

| Parameter  | Value                     |
|--|---------------------------|
| Alternative name <sup>a</sup>                          | TYC 2689-70-1             |
| Alternative name <sup>b</sup>                          | TOI-1456                  |
| R.A. (J2000)   | 20:26:57.92               |
| Dec. (J2000)   | +33:44:40.02              |
| Parallax (mas) <sup>c</sup>                            | $12.37 \pm 0.03$          |
| V magnitude <sup>a</sup>                               | $8.56 \pm 0.01$           |
| Effective temperature (K) <sup>d</sup>                 | $6089^{+97}_{-96}$        |
| Surface gravity (dex) <sup>d</sup>                     | $4.279^{+0.027}_{-0.034}$ |
| Metallicity (dex) <sup>d</sup>                         | $0.036^{+0.059}_{-0.058}$ |
| Stellar mass ( $M_{\odot}$ ) <sup>d</sup>              | $1.127 \pm 0.077$         |
| Stellar radius ( $R_{\odot}$ ) <sup>d</sup>            | $1.277^{+0.039}_{-0.036}$ |
| Age (Gyr) <sup>d</sup>                                 | $4.3^{+2.5}_{-1.9}$       |
| Period (days) <sup>d</sup>                             | $18.71204 \pm 0.00043$    |
| Eccentricity <sup>d</sup>                              | $0.032^{+0.030}_{-0.022}$ |
| Planetary mass ( $M_{\text{Jupiter}}$ ) <sup>d</sup>   | $0.244 \pm 0.021$         |
| Planetary radius ( $R_{\text{Jupiter}}$ ) <sup>d</sup> | $0.867^{+0.027}_{-0.025}$ |

<sup>a</sup> Høg et al. (2000).

<sup>b</sup> Guerrero et al. (2021).

<sup>c</sup> Gaia Collaboration et al. (2018).

<sup>d</sup> Dalba et al. (2020).

After correcting for the background light, there are still some systematics present. In an attempt to mitigate this, we firstly remove the transits using the best-fitting parameters from Dalba et al. (2020) as shown as the gray line in the top panel of Fig. 1. We then applied a Savitsky-Golay filter (Savitzky & Golay 1964) as implemented in *lightcurve* shown as the gray line in the middle panel. We then removed the outliers shown as red points also in the middle panel of Fig. 1. After having corrected and cleaned the light curve we re-injected the transit, which can be seen in the bottom panel. Here we have highlighted points 7 hr before and after mid-transit in orange, blue, and green, which are the data points we use in our fit.

To determine the projected obliquity in HD 332231 we obtained spectroscopic transit data with the High Accuracy Radial velocity Planetary Searcher North (HARPS-N; Mayor et al. 2003; Cosentino et al. 2012) mounted on the 3.58 m Telescopio Nazionale Galileo (TNG) located on Roque de los Muchachos, La Palma, Spain. We observed a transit occurring during the night 4th August, 2020 with observations starting at 21:05 UT until 03:40 UT (programme ID: A41/TAC19, P.I. Knudstrup). The exposure time was set to 540 s and with an overhead of roughly 20 s, the sampling was approximately 560 s. For comparison the total transit lasts about 6.1 hr. The Radial Velocities (RVs) and  $1\sigma$  uncertainties obtained through the Data Reduction Software (DRS) of HARPS-N are printed in Table A.1 and shown in Fig. 2, top panel. The middle panel shows the Signal-To-Noise (S/N) for each exposure for three orders and the airmass, ranging from 1.4 to 1.0, is plotted in the lower panel along with the airmass of the Moon plotted as a dashed line. The seeing was variable with values between 0.9 and 2.0 arcsec with a median of 1.5 arcsec.

We supplement our HARPS-N transit observations with the RVs presented in Dalba et al. (2020). These include RVs obtained using the Levy Spectrograph (Radovan et al. 2010) at the Automated Planet Finder (APF; Radovan et al. 2014; Vogt et al. 2014), the High Resolution Echelle Spectrometer (HIRES; Vogt et al. 1994) at the Keck I telescope, and the Hertsprung node of

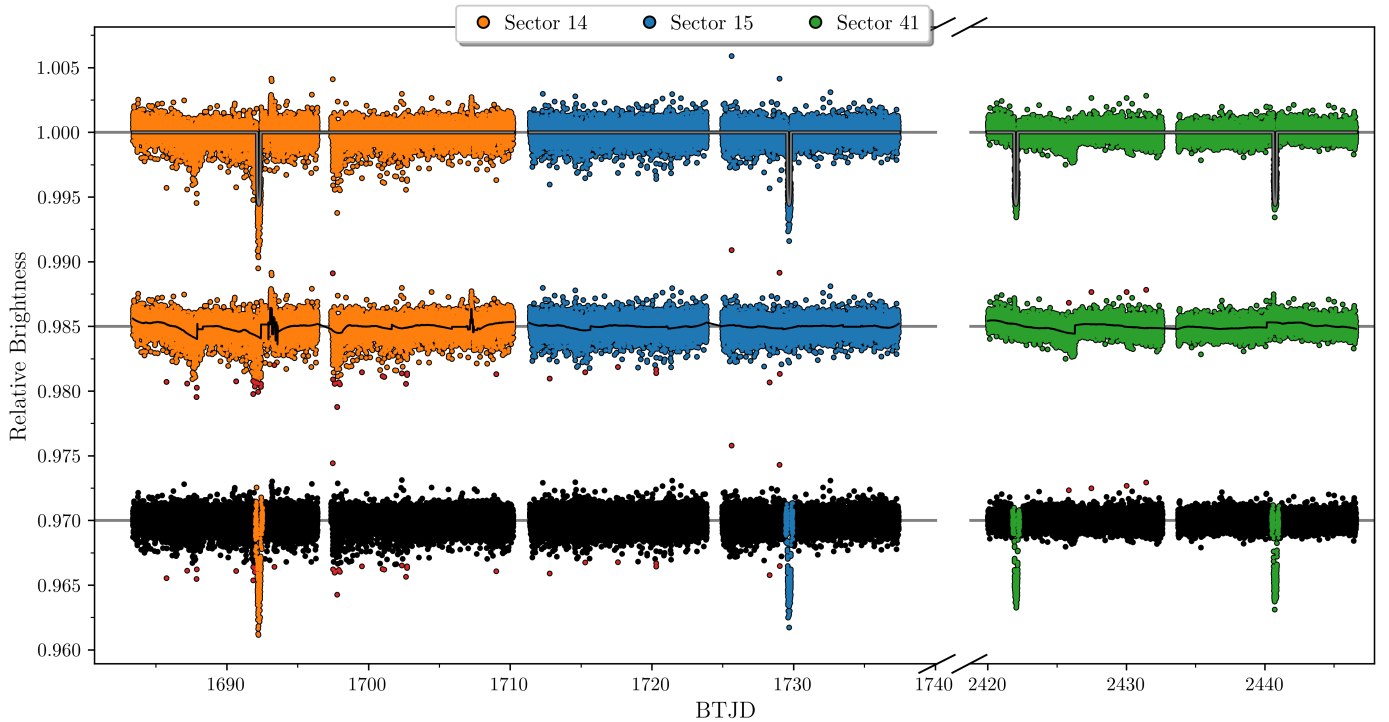


**Fig. 1.** The top light curve shows the normalised, but not detrended, light curve of HD 332231 as observed by TESS in orange, blue, and green points corresponding to Sector 14, Sector 15, and Sector 41, respectively. The gray line is a transit model created from the parameters in Dalba et al. (2020). The transit model has been used to temporarily remove the transit in the light curve offset by -0.015 (denoted as the straight line below the points). Here the gray line shows a Savitsky-Golay filter (as implemented in Lightkurve Collaboration et al. 2018) used to filter and de-trend the data. The red points are outliers removed through a  $5\sigma$  sigma clipping. The filtered, de-trended data with outliers removed and the transits re-injected is shown in the black light curve offset by -0.03. Here the coloured points are snippets of around 7.0 hr of mid-transit, the TESS data used in the remainder of this work.

the Stellar Observations Network Group (SONG; Andersen et al. 2014; Grundahl et al. 2017). The RVs from Dalba et al. (2020) as well as our HARPS-N observations are shown in Fig. 3.

### 3. Determining the projected stellar obliquity in the HD 332231 system

When part of the rotating stellar surface is blocked from view then the rotational broadened stellar absorption lines are distorted relative to their uneclipsed shape. The distortion and its time evolution are governed by the projection of the angle between the stellar spin axis and the orbital angular momentum of the occulting body.

Using the HARPS-N data from the night on the 4th August, 2020 supplemented by the TESS photometry and the publicly available RV data described above, we measure  $\lambda$  employing three different approaches. We are motivated to do so as different analysis methods can have different dependencies on systematics towards some system parameters, e.g., timing offsets and orbital inclination. We used the following approaches: i) We analyzed the stellar absorption lines and distortions thereof during the transits itself. For this we use the Cross-Correlation Function CCF, serving as an "average stellar absorption line" as delivered by the DRS. ii) We also employ a procedure where we first measure the position of the CCF distortion in RV space, and then use these subplanetary velocities,  $v_p$ , to determine the projected obliquity. iii) Finally, we determine the projection of  $\psi$  using the anomalous stellar RVs occurring during transit as a result of the line distortions. As all three methods use the same data sets, they should all deliver fully consistent results.

Before describing the specific steps for each approach we outline the setup common to all three approaches. In each case we create a model which we compare to the data sets, the spectroscopic the transit data, TESS photometry and RVs taken outside transits. We extract the confidence intervals of relevant parameters using a Monte Carlo Markov Chain (MCMC) as described below.

Parameters mainly governed by photometric data are the orbital period,  $P$ , a specific mid-transit point,  $T_0$ , planet to star radius ratio,  $r/R$ , the scaled semi-major axis,  $a/R$ , the cosine of the orbital inclination,  $\cos i_o$ , and the quadratic limb darkening parameters,  $q_1$  and  $q_2$ . For all three approaches to determine the projected obliquity we model the TESS lightcurves with the Mandel & Agol (2002) formalism as implemented in the *batman* package (Kreidberg 2015). For reasons discussed in parameter in Section 4 we also included here in our final model to data comparison one additional parameter,  $\Delta T_0$ . This parameter allows the spectroscopic transit midpoint to float with respect to the midpoint given by the linear ephemeris ( $P, T_0$ ).

Parameters mainly determined by out of transit RVs are the orbital RV semi-amplitude,  $K$ , the orbital eccentricity,  $e$ , the argument of periastron,  $\omega$ , and the RV offsets for the four spectrographs,  $\gamma_i$  ( $i$  = HARPS-N, Levy, HIRES, SONG), as well as their RV jitter terms added in quadrature to the RV uncertainties provided by the RV pipelines  $\sigma_i$ . Parameters describing the shape of the CCFs and any distortions during transits are the projected stellar rotation speed,  $v \sin i$ , stellar surface motion here parametrized by macro-turbulence,  $\zeta$ , and micro-turbulence,  $\xi$  (Gray 2005). The HARPS-N instrument provides spectra with a resolution of  $R \approx 115\,000$  resulting in a spectral Point Spread

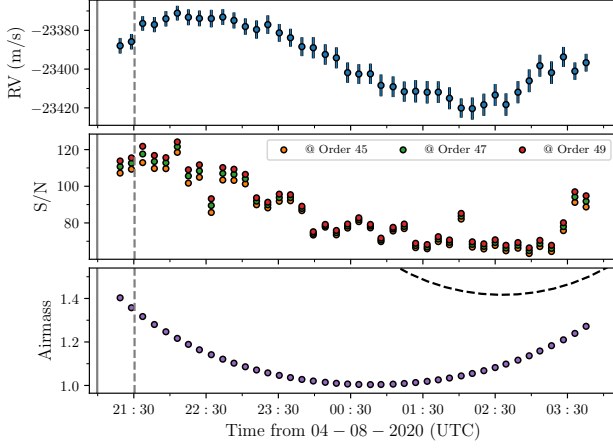


**Fig. 2.** **Top:** The RVs extracted from the HARPS-N pipeline plotted against time. **Middle:** The signal-to-noise for each exposure at three different orders, namely 45, 47, and 49. **Bottom:** The airmass for each exposure is plotted with the airmass of the Moon plotted as the dashed line. In each panel the vertical solid and dotted lines denote nautical and astronomical twilight, respectively.

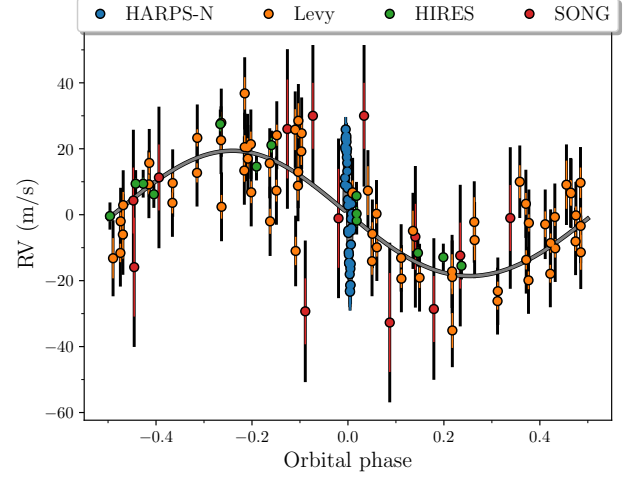


**Fig. 3.** The radial velocities from HARPS-N, Levy, HIRES, and SONG shown with blue, orange, green, and red error bars, respectively. The gray line is the best-fitting model of the orbit modulated by the Rossiter-McLaughlin effect, which is obscured by the HARPS-N data. The colored error bars are the nominal errors, and the black error bar is the nominal error with the jitter term added in quadrature.

Function (PSF) with a FWHM of  $\sim 2.6 \text{ km s}^{-1}$  or a  $\sigma_{\text{PSF}}$  of  $\sim 1.1 \text{ km s}^{-1}$ . We use this value to create a Gaussian with which we convolve our model CCFs. In addition two parameters with which we attempt to capture the limb darkening in the band pass of HARPS-N,  $q_{1,\text{HARPS-N}}$  and  $q_{2,\text{HARPS-N}}$ , are required.

The deformation of the lines during the transit in our model is chiefly governed by the projected obliquity,  $\lambda$  (our parameter of main interest), the above mentioned  $v \sin i$ , and the impact parameter  $b \equiv a/R \cos i_0$ , which is also controlled by the photometric data obtained during transit.

To obtain confidence intervals for our system parameters we employ next to the data described in Section 2 prior information on stellar limb-darkening and stellar surface fields. With the stellar parameters determined by Dalba et al. (2020) and listed in Table 1 we queried the tables provided by Claret et al. (2013) and Claret (2017) for values for quadratic limb-darkening parameters. For the TESS passband we find  $q_1 = 0.253$  and  $q_2 = 0.289$ , for the V band used for our spectroscopic transit data we obtain  $q_{1,\text{HARPS-N}} = 0.513$  and  $q_{2,\text{HARPS-N}} = 0.199$ . From  $T_{\text{eff}}$ ,  $\log g$ , and the relationship presented in Doyle et al. (2014) we find  $\zeta = 4.46 \text{ km s}^{-1}$ . Assuming a sigma of  $1 \text{ km s}^{-1}$  we use this as a Gaussian prior. For the micro-turbulence parameter  $\xi$  we assume a Gaussian prior with a mean of  $2 \text{ km s}^{-1}$  and a  $\sigma$  of  $1 \text{ km s}^{-1}$ , which is in line with the value given in Hirano et al. (2011). All parameters and their priors can be found in Table 2.

Before we can proceed with creating a model and compare it to our data two additional steps concerning the HARPS-N CCFs are required. As mentioned above the PSF of HARPS-N has a  $\sigma_{\text{PSF}}$  of  $\sim 1.1 \text{ km s}^{-1}$ . The CCFs provided by the DRS are sampled on a velocity grid with a bin size of  $0.25 \text{ km s}^{-1}$ . We therefore bin the CCFs onto a velocity scale with  $1 \text{ km s}^{-1}$  wide bins. Secondly, to assign the proper weight to each type of data (photometry, out of transit RVs, HARPS-N transit night data) the different data sets require properly scaled uncertainties. To obtain such uncertainties for the CCFs we performed a fit to the last three CCFs obtained during the transit night, as these have been obtained after egress. The averaged out-of-transit (OOT) CCF was fitted with the relevant parameters from above ( $v \sin i$ ,  $\zeta$ ,  $\xi$ ,

and limb-darkening). From this best fit and requiring a reduced chi-squared,  $\chi^2_r$ , to be  $\approx 1$  we obtain uncertainties of  $\sim 0.0004$  for each velocity point in the CCF. Furthermore, we normalize our CCFs by setting the surface area under the CCF to 1 for both data and model. In Fig. 4 we display the OOT CCFs, the best fitting model and residuals of the CCFs. We are now in a position to compare the data to the different models.

### 3.1. Line distortions - planet shadow

Here we analyze the deformations of the stellar lines caused by the planetary transits directly. To do so we follow the approach by Albrecht et al. (2007, 2013); Hjorth et al. (2021), but see also, e.g., Brown et al. (2012); Johnson et al. (2014); Zhou et al. (2016). Our model CCFs are created by constructing a limb-darkened stellar grid, where we assume a quadratic limb darkening law of the form

$$I = 1 - u_1(1 - \mu) - u_2(1 - \mu)^2. \quad (1)$$

Here  $\mu = \cos(\theta)$  with  $\theta$  being the angle between the local normal and a line parallel to the line of sight.  $I$  is the local intensity normalized by the intensity at the center of the disk, i.e.,  $\mu = 1$ .

For each pixel of the stellar surface we include the effects of macro- and micro-turbulence following Gray (2005). The local line profile in our model is then given by

$$\Theta(v) = \frac{1}{2\sqrt{\pi}\zeta} \left( \frac{\exp(-v/\zeta \cos \theta)^2}{\cos \theta} + \frac{\exp(-v/\zeta \sin \theta)^2}{\sin \theta} \right), \quad (2)$$

where we have assumed equal velocities and surface areas for tangential and radial flows.

Assuming solid body rotation (no differential surface rotation) the radial velocity of the stellar surface is a function of the distance from the stellar spin axis only. We define a coordinate system so that the  $x$ -axis is oriented along the stellar equator and the  $y$ -axis parallel to the projected stellar spin axis. The Doppler velocity of the stellar surface below a planet  $v_p$  is then simply given by the distance from the  $y$ -axis and the projected stellar

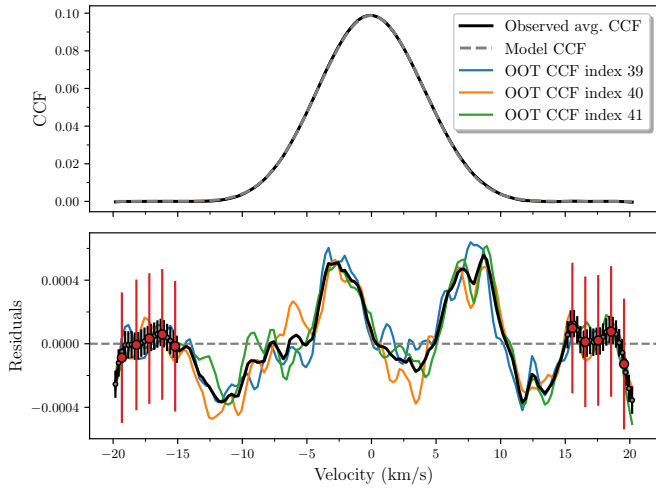


**Fig. 4. Top:** The average (created from the three out-of-transit CCFs) observed CCF shown as the solid black line with the best-fitting model overlain as the gray dashed line. The surface area under the CCF was arbitrarily set to 1. All CCFs have been shifted into the stellar rest frame. **Bottom:** The residuals between the OOT CCF and model. We also show the three epochs used to create our average out of transit CCF, i.e., the three last observations on the 4th August, 2020 (Indexing started with 0). Shown as gray error bars is the scatter on the CCFs outside of the central peak, specifically  $\pm 15 \text{ km s}^{-1}$ , which we have binned to  $1 \text{ km s}^{-1}$  and scaled to get a  $\chi^2_\nu \sim 1$ . The binned and scaled errors are shown with red error bars, which are applied to all data points, but for illustrative purposes only shown in the aforementioned range.

rotation speed,

$$v_p = \frac{x}{R} v \sin i. \quad (3)$$

The position of the planet ( $x_p, y_p$ ) in this coordinate system is given by

$$\begin{pmatrix} x_p \\ y_p \end{pmatrix} = \begin{pmatrix} -\frac{\Gamma}{R} \cos(\omega + \nu) \\ -\frac{\Gamma}{R} \sin(\omega + \nu) \cos i_o \end{pmatrix} \begin{pmatrix} \cos \lambda & -\sin \lambda \\ \sin \lambda & \cos \lambda \end{pmatrix}. \quad (4)$$

Here  $\nu$  represents the true anomaly and  $\Gamma$  the distance between the centers of the planet and star on the Keplerian orbit.<sup>1</sup> The matrix is simply the 2D rotation matrix for the angle  $\lambda$ .

In our model we can now calculate for each observations if parts of the rotating stellar disk are blocked from view. We perform this calculation for each observation and set the flux of pixels covered by the planet to zero when we integrate over the visible stellar surface to obtain a model of the stellar line at particular phases of the transit. Next the lines are convolved with a Gaussian which width is given by the quadrature sum of  $\xi$  and  $\sigma_{\text{PSF}}$ . Finally the model CCFs are shifted in velocity space according to a Keplerian model. For integration times long enough so the planets movement over the stellar disk is  $\geq r/R$  "phase smearing" occurs. Data should then be compared to models which are integrated over such time intervals to emulate phase smearing. For the current set of observations the exposure time to transit duration ratio is  $\approx 0.02$ , less than  $r/R \approx 0.07$ . We therefore do not take this into account here.

Now the model CCFs are compared to the observed CCFs. As in Albrecht et al. (2013) we also try to mitigate changes in the Signal-to-Noise Ratio (SNR) throughout the night might have

<sup>1</sup> Normally the orbital distance is indicated by  $r$ , which we have assigned to the planetary radius.

on the normalization of the spectra and resulting CCFs. Such changes might lead to slightly different SNRs in the CCFs and therefore slightly different CCF heights as well as small overall changes in the CCF baseline. We assign three parameters to each CCF, an intensity offset, a slope, and a scalar. These parameters are optimized every time a model is compared to the data. This approach serves to propagate the effects of any potential changes in the normalization into the confidence intervals of final system parameters. In the case of our particular data set, however, these parameters vary by less than 0.01% throughout the night as the transit spectra had been taken under good and relatively stable conditions (Section 2) by a fiber fed spectrograph.

In Fig. 5 we show the best-fitting light curve from the MCMC (Section 3.4), while in Fig. 6 a) we show the HARPS-N data with the best-fitting model as well as the residuals. Here we subtracted the OOT CCF to highlight the deformation due to the planetary transit onto the CCFs. The planetary shadow first covers the blueshifted light and during the second half of the transit the redshifted light, consistent with a prograde transit.

### 3.2. Subplanetary Velocity

A second approach to measure  $\lambda$  is to determine the subplanetary velocity,  $v_p$ , for each observation and then use a simple geometric model to determine  $\lambda$  from the  $v_p$  measurements (e.g., Cegla et al. 2016; Hoeijmakers et al. 2020). The results of this method do not depend directly on surface velocity fields. A dependence does remain as the OOT CCFs supply information on  $v \sin i$ , and that  $v \sin i$  measurement does depend on the surface velocity fields. This additional information on  $v \sin i$  is particular important for our system as the impact parameter is close to zero (see Albrecht et al. 2011, for a discussion on this dependency).

The subplanetary velocities are obtained in the following way: The OOT CCF, shifted to the appropriate velocities, is subtracted from the in-transit CCFs. This isolates the distortion in the stellar lines, i.e., the planet shadow. The central subplanetary velocity is then measured by fitting a Gaussian to the distortions during transit, where we only searched for a distortion of the CCFs inside the interval  $\pm 2 \times v \sin i$ . We used the uncertainties derived from the co-variance matrix of a Levenberg-Marquardt fit and then further increased them in quadrature so  $\chi^2_\nu \approx 1$ . We extract  $v_p$  for each set of system parameters afresh out of concern that any error we make in isolating the planet shadow by – for example not using the proper orbital velocity – might lead to a systematic error in the measured  $v_p$ . However, we have tested that even for line parameters significantly outside our confidence intervals the subtraction of the overall line and subsequent determination of  $v_p$  does not change  $v_p$  outside its uncertainty interval. The extracted velocities and their uncertainties are given in Table A.1 and can be seen in Fig. 6 b).

From Eq. (3) it is clear that  $v_p$  only depends on the  $x$  coordinate of the planet and should progress linearly with time. Therefore in our model we can calculate  $v_p$  with a first order polynomial, which extremes occur at ingress  $V_{\text{ingress}}$  and  $V_{\text{egress}}$  and both being taken as positive values. The offset and amplitude of the line are given by (Albrecht et al. 2011, Albrecht et al. in prep),

$$\begin{aligned} V_{\text{egress}} - V_{\text{ingress}} &= 2 \times (v \sin i) \sin \lambda \times b, \\ V_{\text{egress}} + V_{\text{ingress}} &= 2 \times (v \sin i) \cos \lambda \times \sqrt{1 - b^2}. \end{aligned} \quad (5)$$

For this particular system with  $b \approx 0$  good alignment would be indicated with  $V_{\text{egress}} + V_{\text{ingress}} \approx 2 \times (v \sin i) \approx 11 \text{ km s}^{-1}$ .



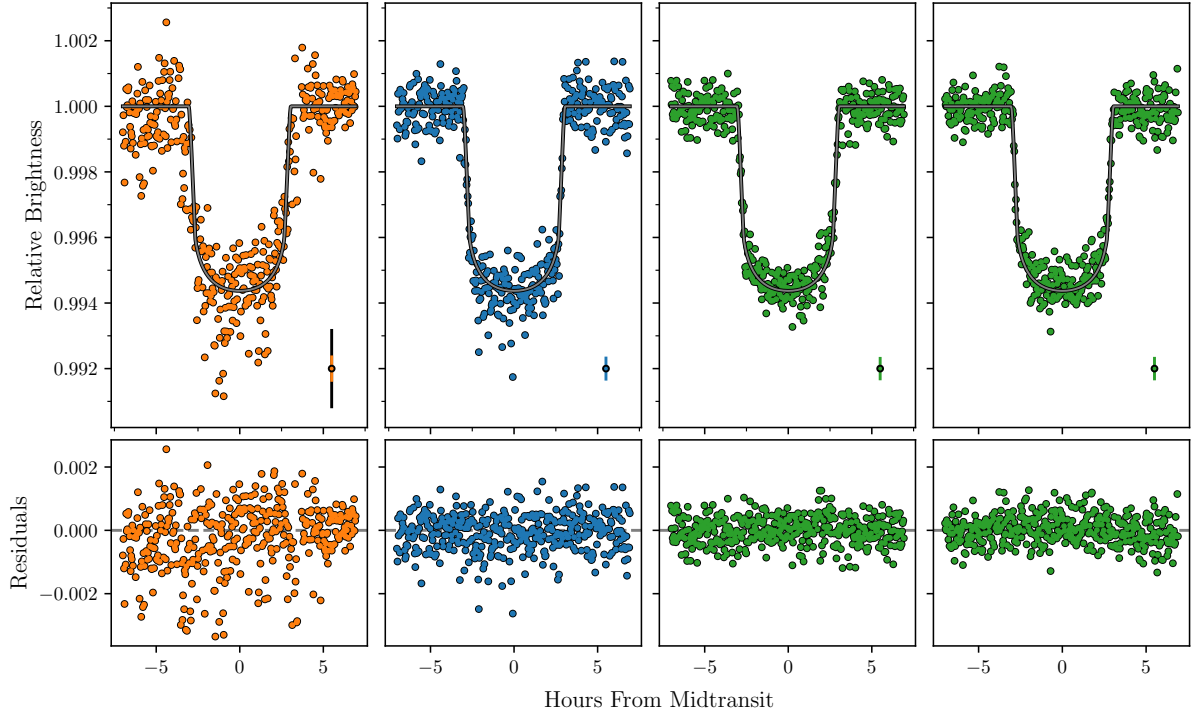


**Fig. 5. Top:** The transit data points from the TESS light curve in Fig. 1 used in the fit. The gray line is the best-fitting light curve model. **Bottom:** The residuals from subtracting the best-fitting model from the data. In each top panel we show an error bar that is representative of the error from this particular snippet of data. Note that for the Sector 14 data we have added the photometric jitter in quadrature (shown in black) to the nominal error (orange).

### 3.3. Radial Velocities

The distortions of the spectral lines as seen in Fig. 6 a) lead to anomalous RVs observed during transit, displayed in Fig. 6 c). A first order estimate of the anomalous stellar RVs can be obtained from

$$RV_{RM}(t) \approx -\left(\frac{r}{R}\right)^2 v_p(t). \quad (6)$$

The  $RV_{RM}$  measurements relate to  $v_p$  and the radii ratio of the transiting to the occulted object. The sign change occurs as the subplanetary light is blocked from view. Any particular  $RV_{RM}$  is further modified by the stellar limb darkening at the subplanetary point on the stellar disk, Eq. (1), and during ingress and egress by the ratio of the planetary disk in front of the star. Compare Fig. 6 b) to Fig. 6 c). For our RV model we used the algorithm by Hirano et al. (2011) which also includes the effect of instrumental and stellar broadening. As for the other two approaches we also here include a Keplerian RV model.

### 3.4. Data to model comparison

To extract confidence intervals for the system parameters we use MCMCs. We define our likelihood function as,

$$\log \mathcal{L} = -0.5 \sum_{i=1}^N \left[ \frac{(O_i - C_i)^2}{\sigma_i^2} + \log 2\pi\sigma_i^2 \right] + \sum_{j=1}^M \log \mathcal{P}_j, \quad (7)$$

where  $N$  indicates the total number of data points from photometry, archival RVs, and the spectroscopic data obtained during the

transit night.  $C_i$  represents the model corresponding to the observed data point  $O_i$ .  $\sigma_i$  is the uncertainty for the  $i$ th data point, where we add a jitter term in quadrature and a penalty in the likelihood for the RVs as well as Sector 14 photometry, which as mentioned is heavily affected by systematics.  $\mathcal{P}_j$  denotes the prior for the  $j$ th parameter listed in Table 2.

We did not step directly in the limb-darkening coefficients, rather we were stepping in the sum of the two, i.e.,  $q_1 + q_2$ , where we applied a Gaussian prior with a width of 0.1. The difference, i.e.,  $q_1 - q_2$ , was kept fixed during the sampling. Furthermore, our MCMC was stepping in  $\sqrt{e} \cos \omega$ ,  $\sqrt{e} \sin \omega$ , and  $\cos i$ . We use emcee (Foreman-Mackey et al. 2013) to carry out the Markov Chain Monte Carlo (MCMC) sampling of the posteriors. To ensure that our MCMC runs have converged, we invoke the rank normalised  $\hat{R}$  diagnostic test (Vehtari et al. 2019) using the rhat module implemented in ArviZ (Kumar et al. 2019). Our results for all three approaches are given in Table 2, and all clearly suggest that the stellar spin axis and the orbital axis of the planet are aligned.

## 4. Results

The additional TESS photometry from Sector 41 allows us to improve the planet-to-star radius ratio compared to the discovery paper shrinking the uncertainty by  $\sim 60\%$ . We find  $r/R = 0.07004^{+0.00015}_{-0.00014}$ . This is because i) now four instead of two transits have been observed and ii) Sector 41 photometry has a lower scatter. Using our new value for  $r/R$  with the stellar radius given in Dalba et al. (2020, see our Table 1), we find

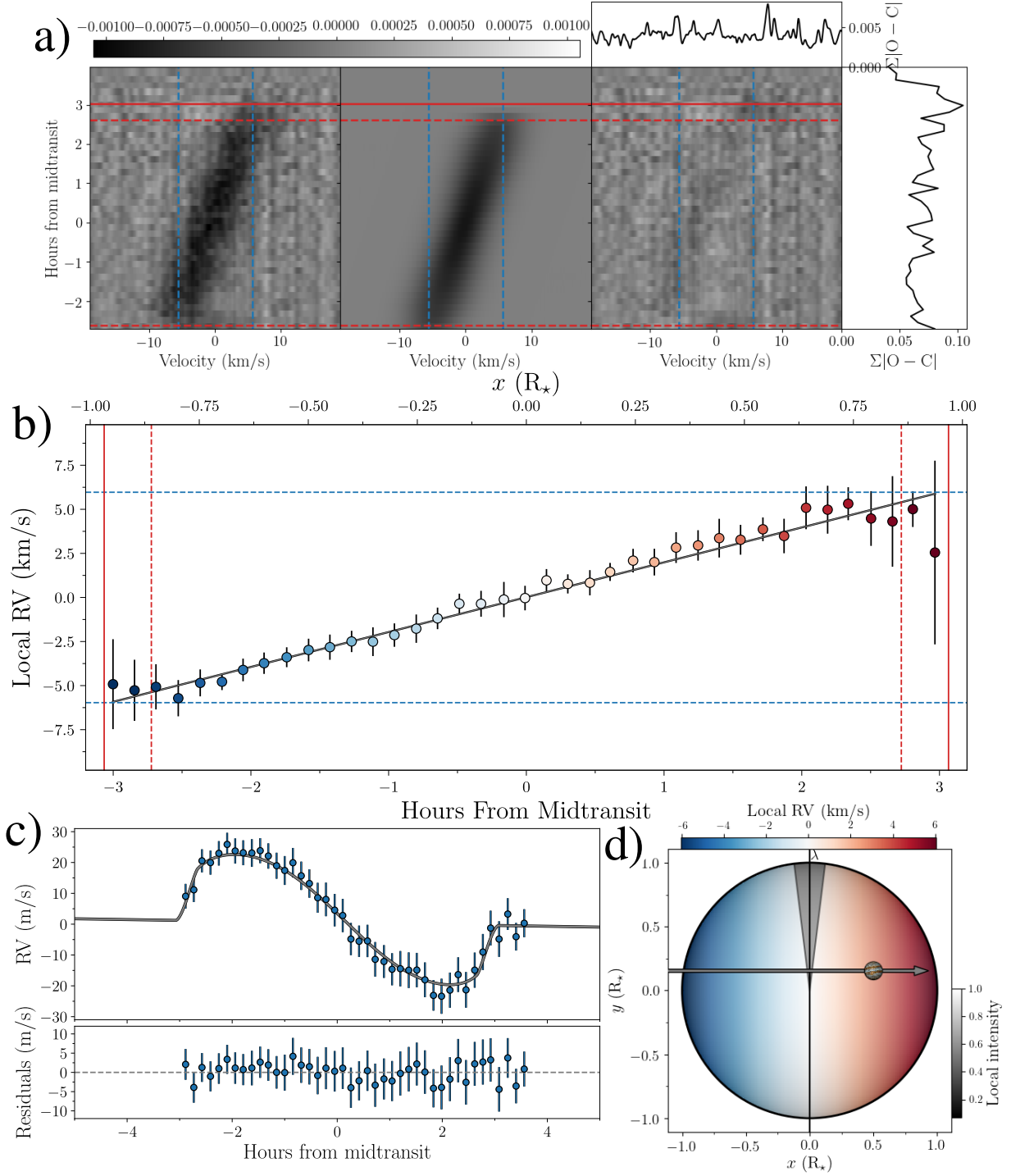


**Fig. 6. a) Left:** The distortion of the stellar absorption lines as observed with HARPS-N during the transit night. The vertical lines denote  $\pm v \sin i$ . The horizontal dashed lines are the second and third contact, i.e., the times in between is when the planet is completely within the stellar disk, and the solid line is the fourth contact, i.e., the point where the stellar and planetary disks no longer overlap. **Middle:** The best-fitting model of the distortion of the absorption lines. **Right:** The residuals from subtracting the best-fitting model from the data with the summed values displayed on top and to the right. In all panels data and model have been shifted into the stellar restframe, a minor effect. The horizontal colour bar on top denotes the strength of the signal. **b)** The subplanetary, or local, RVs created by subtracting the out of transit CCF from the in-transit ones and measuring the position of the excess bump caused by the planet. The error bars are colour-coded according to the  $v \sin i$  value they should have given their  $x$ -position in **d)**, which shows the orientation of the orbit and the projected stellar rotation going from blue ( $-v \sin i$ ) to red ( $v \sin i$ ). As in **a)** the dashed blue line denotes the value for  $v \sin i$ , while the solid and dashed red lines mark the contact points. **c) Top:** Shown with blue error bars are the radial velocities from HARPS-N used in the fit. The gray line is the best-fitting model of the Rossiter-McLaughlin effect. **Bottom:** The residuals from subtracting the best-fitting model from the data. **d)** The geometry of the system with the planet transiting the rotating and limb-darkened star, which is tilted by  $\lambda$  with respect to the orbit of the planet marked with the gray arrow. The horizontal colour bar shows the rotation speed at a given longitude, and the gray colour bar shows the relative intensity given going from 1.0 in the center to around 0.16 at the limb (given the limb-darkening parameters for HARPS-N in Table 2). Here the intensity overlay has been made transparent to make the rotation colour-coding visible.

**Table 2.** Results from the MCMCs using the RVs, the planet shadow, and the local sub-planetary velocity. The value is the median of the samples and the upper and lower uncertainties are estimated from the highest posterior density at a confidence level of 0.68. We denote the uniform priors as  $\mathcal{U}$  and the Gaussian priors with a mean,  $\mu$ , and width,  $\sigma$ , as  $\mathcal{N}(\mu, \sigma)$ . We chose the parameters obtained from analyzing the deformation in the lines (the planetary shadow) as our final parameters.  $T_0$  is given in TESS Barycentric Julian Date (BTJD; BJD – 2457000).

| Parameter                       | Prior                      | RV                                  | Shadow                          | Slope                               |
|---------------------------------|----------------------------|-------------------------------------|---------------------------------|-------------------------------------|
| Stepping parameters             |                            |                                     |                                 |                                     |
| $P$ (days)                      | $\mathcal{U}$              | $18.712062^{+0.000009}_{-0.000008}$ | $18.712062 \pm 0.000009$        | $18.712062^{+0.000009}_{-0.000008}$ |
| $T_0$ (BTJD)                    | $\mathcal{U}$              | $1729.6810 \pm 0.0003$              | $1729.6810^{+0.0003}_{-0.0002}$ | $1729.6810 \pm 0.0003$              |
| $\Delta T_0$ (min.)             | $\mathcal{U}$              | $20 \pm 3$                          | $18 \pm 3$                      | $23 \pm 4$                          |
| $r/R$                           | $\mathcal{U}$              | $0.07005^{+0.00016}_{-0.00015}$     | $0.07003^{+0.00015}_{-0.00014}$ | $0.07004^{+0.00014}_{-0.00015}$     |
| $a/R$                           | $\mathcal{U}$              | $24.4^{+0.4}_{-0.3}$                | $24.5^{+0.3}_{-0.2}$            | $24.5^{+0.4}_{-0.2}$                |
| $\cos i$                        | $\mathcal{U}$              | $0.0033^{+0.0015}_{-0.0033}$        | $0.0026^{+0.0013}_{-0.0026}$    | $0.0026^{+0.0012}_{-0.0026}$        |
| $K$ (m/s)                       | $\mathcal{U}$              | $17.5^{+1.2}_{-1.1}$                | $17.5^{+1.2}_{-1.1}$            | $17.5^{+1.2}_{-1.1}$                |
| $\sqrt{e} \cos \omega$          | $\mathcal{U}$              | $0.10^{+0.12}_{-0.09}$              | $0.12^{+0.12}_{-0.09}$          | $0.11^{+0.13}_{-0.09}$              |
| $\sqrt{e} \sin \omega$          | $\mathcal{U}$              | $0.09^{+0.05}_{-0.06}$              | $0.09^{+0.05}_{-0.06}$          | $0.09^{+0.05}_{-0.06}$              |
| $\sigma_{\text{Sector 14}}$     | $\mathcal{U}$              | $0.00095 \pm 0.00004$               | $0.00095 \pm 0.00004$           | $0.00095 \pm 0.00004$               |
| $\gamma_{\text{HARPS-N}}$ (m/s) | $\mathcal{U}$              | $-23395.2^{+1.1}_{-1.0}$            | $-23346 \pm 12$                 | $-23344^{+12}_{-13}$                |
| $\sigma_{\text{HARPS-N}}$ (m/s) | $\mathcal{U}$              | $0.6^{+0.3}_{-0.6}$                 | -                               | -                                   |
| $\gamma_{\text{Levy}}$ (m/s)    | $\mathcal{U}$              | $1.1^{+1.2}_{-1.1}$                 | $1.0 \pm 1.2$                   | $1.1^{+1.1}_{-1.2}$                 |
| $\sigma_{\text{Levy}}$ (m/s)    | $\mathcal{U}$              | $8.7^{+0.9}_{-1.0}$                 | $8.7^{+0.9}_{-1.0}$             | $8.7^{+0.9}_{-1.0}$                 |
| $\gamma_{\text{HIRES}}$ (m/s)   | $\mathcal{U}$              | $-1.6 \pm 1.1$                      | $-1.6^{+1.0}_{-1.2}$            | $-1.6 \pm 1.1$                      |
| $\sigma_{\text{HIRES}}$ (m/s)   | $\mathcal{U}$              | $3.4^{+0.9}_{-1.1}$                 | $3.5^{+0.8}_{-1.2}$             | $3.5^{+0.9}_{-1.1}$                 |
| $\gamma_{\text{SONG}}$ (m/s)    | $\mathcal{U}$              | $2 \pm 6$                           | $2 \pm 6$                       | $2 \pm 6$                           |
| $\sigma_{\text{SONG}}$ (m/s)    | $\mathcal{U}$              | $18^{+5}_{-6}$                      | $18^{+4}_{-6}$                  | $18^{+5}_{-6}$                      |
| $q_1 + q_2$ : TESS              | $\mathcal{N}(0.542, 0.1)$  | $0.511^{+0.020}_{-0.019}$           | $0.511^{+0.019}_{-0.020}$       | $0.509^{+0.020}_{-0.019}$           |
| $q_1 + q_2$ : HARPS-N           | $\mathcal{N}(0.7114, 0.1)$ | $0.78^{+0.08}_{-0.09}$              | $0.77 \pm 0.09$                 | $0.87^{+0.10}_{-0.09}$              |
| $v \sin i$ (km/s)               | $\mathcal{U}$              | $5.61^{+0.18}_{-0.17}$              | $5.63 \pm 0.11$                 | $5.88^{+0.13}_{-0.14}$              |
| $\zeta$ (km/s)                  | $\mathcal{N}(4.46, 1.0)$   | $4.8 \pm 0.5$                       | $4.7 \pm 0.3$                   | $4.8 \pm 0.2$                       |
| $\xi$ (km/s)                    | $\mathcal{N}(2.0, 1.0)$    | $2.7 \pm 0.3$                       | $2.72^{+0.17}_{-0.20}$          | $2.41^{+0.17}_{-0.18}$              |
| $\lambda$ (°)                   | $\mathcal{U}$              | $-2^{+15}_{-16}$                    | $-1 \pm 7$                      | $0 \pm 7$                           |
| Derived parameters              |                            |                                     |                                 |                                     |
| $i$ (°)                         |                            | $89.81^{+0.19}_{-0.09}$             | $89.85^{+0.15}_{-0.08}$         | $89.85^{+0.15}_{-0.07}$             |
| $b$                             |                            | $0.08^{+0.04}_{-0.08}$              | $0.06^{+0.03}_{-0.06}$          | $0.06^{+0.03}_{-0.06}$              |
| $e$                             |                            | $0.028^{+0.019}_{-0.028}$           | $0.030^{+0.017}_{-0.030}$       | $0.030^{+0.017}_{-0.030}$           |
| $\omega$ (°)                    |                            | $45^{+24}_{-45}$                    | $41^{+23}_{-41}$                | $43^{+24}_{-43}$                    |
| $T_{41}$ (hours)                |                            | $6.129 \pm 0.011$                   | $6.129 \pm 0.010$               | $6.128 \pm 0.010$                   |
| $T_{21}$ (hours)                |                            | $0.404^{+0.003}_{-0.004}$           | $0.403 \pm 0.003$               | $0.403^{+0.002}_{-0.003}$           |
| $r$ ( $R_{\text{Jupiter}}$ )    |                            | $0.870 \pm 0.016$                   | $0.870 \pm 0.016$               | $0.870 \pm 0.016$                   |
| $q_1$ : HARPS-N                 |                            | $0.55^{+0.04}_{-0.04}$              | $0.54^{+0.04}_{-0.04}$          | $0.59^{+0.05}_{-0.05}$              |
| $q_2$ : HARPS-N                 |                            | $0.23^{+0.04}_{-0.04}$              | $0.23^{+0.04}_{-0.04}$          | $0.28^{+0.05}_{-0.05}$              |
| $q_1$ : TESS                    |                            | $0.237^{+0.010}_{-0.009}$           | $0.238^{+0.010}_{-0.010}$       | $0.237^{+0.010}_{-0.010}$           |
| $q_2$ : TESS                    |                            | $0.273^{+0.010}_{-0.009}$           | $0.274^{+0.010}_{-0.010}$       | $0.273^{+0.010}_{-0.010}$           |

$r = 0.870 \pm 0.016 R_{\text{Jupiter}}$ , which is consistent with the discovery value of  $0.867^{+0.027}_{-0.025} R_{\text{Jupiter}}$ .

There is a discrepancy in the systemic velocity for the HARPS-N data,  $\gamma_{\text{HARPS-N}}$ , between the three approaches, Table 2. The shadow and slope approaches give consistent results with each other but not with the RV method. While we have not further investigated this here, we suspect that this disagreement is caused by the simple stellar line model we employ in the shadow and slope approaches. In particular we do not model convective blueshift as done by Albrecht et al. (2012b) using the approach by Shporer & Brown (2011). Therefore, our model of the line shape is fully symmetric, opposite of what we expect for actual stellar absorption lines. While convective blueshift might influence all three approaches the difference in  $\gamma$  probably comes about as the line and slope method fit the line itself and the ve-

locity position of the distortion  $v_p$ , while the RV method does only fit the RVs. Given the fast rotation of the star and the quality of our data convective blueshift might have influenced the result of  $\gamma$  but not significantly the result for  $\lambda$ . Ideally magneto-hydrodynamics simulations of the stellar photosphere should be used to model the lines (Cegla et al. 2016; Dravins et al. 2017). We further note that the values for  $v \sin i$  and  $q_1 + q_2$  : HARPS-N come out a bit larger for the slope compared to the values for the RV and shadow runs. These two parameters are correlated in that for a stronger limb darkening  $v \sin i$  needs to be larger as well to fit the OOT.

Before the recent release of data from TESS' Sector 41, we found in our initial runs that the three approaches of measuring  $\lambda$  lead to inconsistent results. Specifically, the subplanetary velocity approach found alignment ( $\lambda = -7 \pm 8^\circ$ ), the shadow anal-



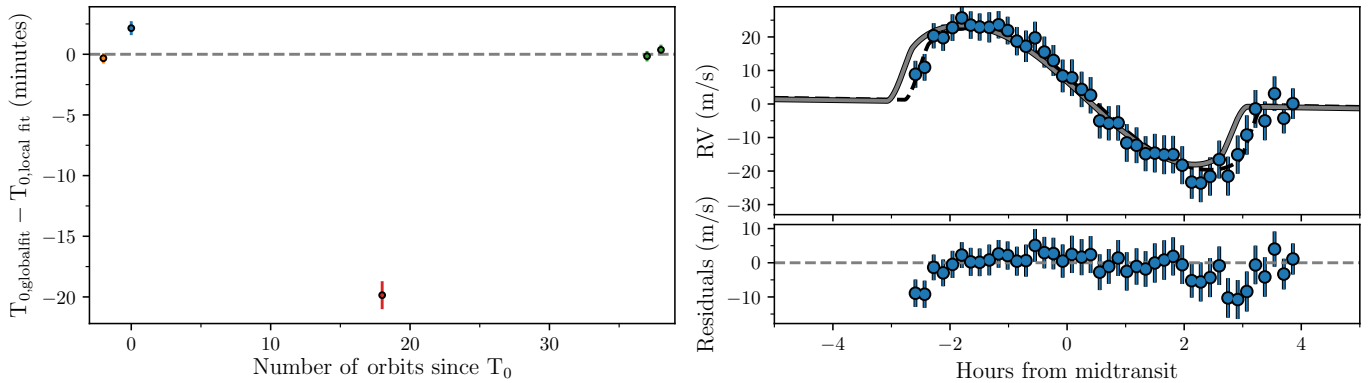


**Fig. 7. Left:** Timing differences between the predictions of transit mid-points derived from linear ephemeris obtained via a global fit to all photometric data and transit mid-points measured for each of the transits individually (now including the spectroscopic transit) i.e.,  $T_0$  from Table 2, and a local fit, where  $T_0$  is free to vary for each of the specific transits. The transits from TESS Sector 14, 15, and 41 are plotted with orange, blue, and green, respectively. The transit observed with HARPS-N is plotted with a red symbol. The spectroscopic transit is offset by several  $\sigma$  from its expected timing. **Right:** Similar to Fig. 6 panel c, but now assuming linear ephemeris resulting in a misaligned ( $\lambda = -31 \pm 6^\circ$ ) orbit shown in gray. Clearly, this model does not fit the data as well as the dashed line, which is the model in panel c of Fig. 6. The lower panel displays the residuals between the linear ephemeris model and data. There are large systematic differences between data and model specifically near ingress and egress, as expected in there is a timing offset.

ysis indicated moderate misalignment ( $\lambda = -16 \pm 4^\circ$ ), and the  $RV_{\text{RM}}$  measurements argued for a highly significant misalignment,  $\lambda = -31 \pm 6^\circ$ .

Including TESS Sector 41 data, we now have photometry obtained during July/August of 2019 and July/August of 2021 bracketing our spectroscopic transit observations from the 4th August, 2020. From this it now appears that the midpoint of the transit we have observed with HARPS-N ( $T_0 = 1729.6810$  in BTJD; TESS Barycentric Julian Date; BJD – 2457000) is shifted by  $\sim 20$  min relative to the expected value from the linear ephemeris as derived from TESS photometry alone. Fig. 7 left panel shows the deviation of the measured transit midpoints from these particular ephemerides.

This apparent mismatch in the mid-transit time had a more significant influence on the result obtained from the RVs than from the shadow and slope. This is because the latter two methods are less governed by ingress and egress data. A shift by a few minutes will lead to a large difference between the  $RV_{\text{RM}}$  model and data (Fig. 7). Such a difference is largest for ingress and egress data. Such data does contribute less to the results for the shadow or slope method and more importantly a shift in timing between model and data can be absorbed into the systemic velocity without influencing the result for  $\lambda$  to much.  $RV_{\text{RM}}$  data – if pre-ingress and/or post-egress data have been obtained – does not allow for such a shift.

We investigated this further by plotting the posteriors for  $P$  and  $T_0$  as obtained from photometry only. We derived these using data from Sectors 14 and 15 only, from Sector 41 only, and from all sectors combined. The results can be seen in Fig. 8. The results from the different sectors appear to be only marginally consistent. Next to  $\lambda$  also other parameters showed inconsistencies. The impact parameter was found to be  $0.23 \pm 0.05$ . This values is inconsistent with the value obtained from photometry alone.

Given these considerations we concluded that a model employing a linear ephemeris is not adequate for modelling the system. However, we do not have enough data to constrain a physical model predicting such Transit Timing Variations (TTVs) for the observed spectroscopic transit. We therefore decided to introduce an additional parameter  $\Delta T_0$ . This parameter allows the

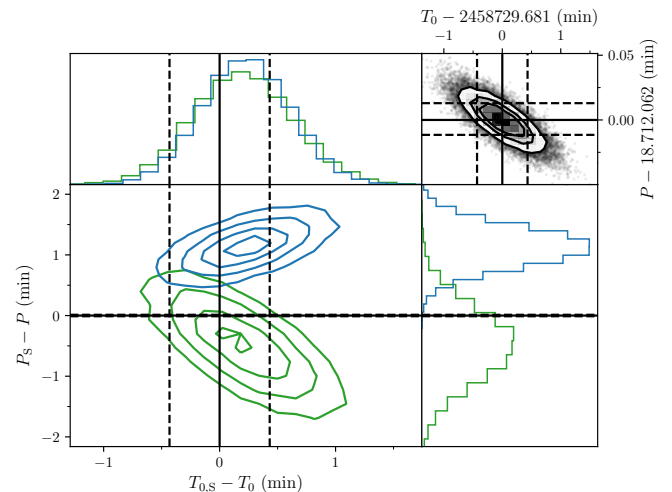


**Fig. 8.** Here we show a fit varying  $P$  and  $T_0$ , but otherwise fixing the parameters from the RV run in Table 2. In blue we only fit the transits in Sector 14 and Sector 15, and in green we only fit the transits from Sector 41. We have subtracted  $P$  and  $T_0$  from Table 2 from the results. Displayed in the top right corner are the posteriors for these, and their values and their confidence intervals are shown as black lines in both correlation plots. Furthermore, we have used that period to shift  $T_0$  from Sector 41, i.e., subtracting  $37 \times P$ . The confidence intervals for the period, translating to different mid-transit points for different epochs is only marginally consistent, indicating the possibility of TTVs.

mid-transit time of the specific transit observed with HARPS-N to float free relative to the prediction from the linear ephemeris, now only determined by the TESS photometry. Adding this additional parameter will reduce the precision of our final result in  $\lambda$  as we ask our spectroscopic data to specify an additional parameter. However, it is a conservative choice as any possible TTVs will now not bias our result for the projected obliquity.

Implementing this change to our model the goodness of the model to data comparison did improve as measured via  $\chi^2$  for all approaches we have employed to determine  $\lambda$ . The most noticeable improvement occurred for the  $\chi^2$  of the RM RV approach

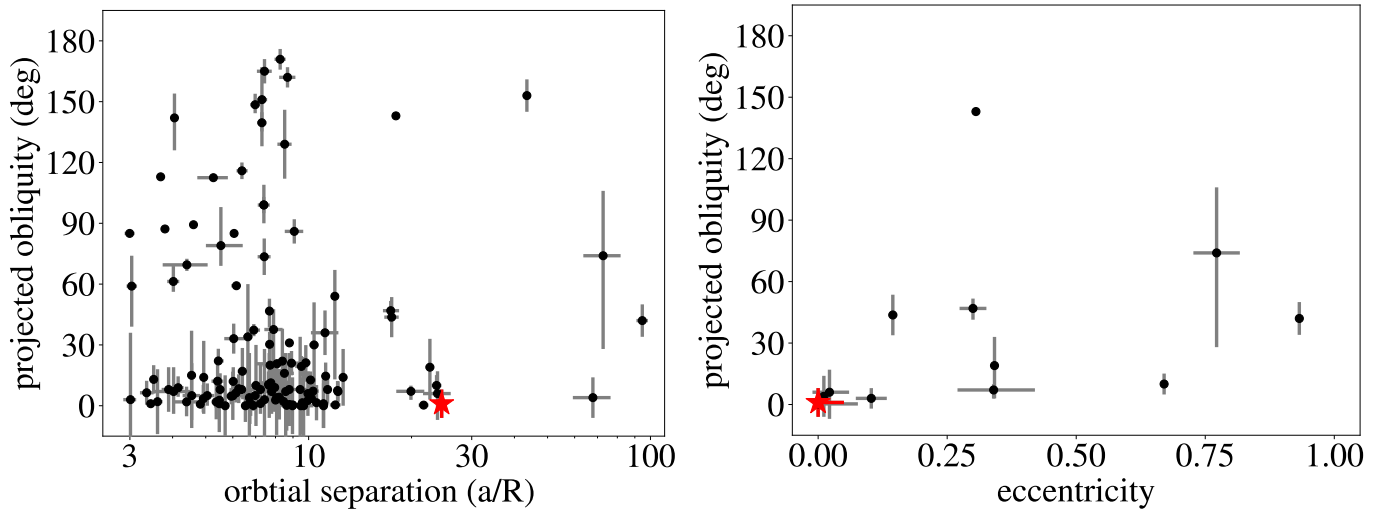


**Fig. 9. Left:** Projected obliquities versus orbital separations **Right:** Projected obliquities versus orbital eccentricities. We only include planets more massive than  $0.2 M_{\text{Jupiter}}$ . In the right panel we further only plots planets on large ( $a/R > 15$ ) orbits and with  $\sigma_{\text{ecc}} < 0.1$ . HD 332231 is marked by a red star, the system belongs to the class of systems with low orbital misalignment, and low orbital eccentricity.

which  $\chi^2$  decreased by factor of  $\approx 2.8$ . More importantly the functional shape of the best fitting RM RV model is a much better fit to the anomalous RVs obtained during transit. This can clearly be seen by comparing the residuals of the right panel in Fig. 7 to Fig. 6 c). Finally, the impact parameters obtained from all three methods now agree, as expected, with the value obtained from photometry alone  $b = 0.10^{+0.04}_{-0.10}$ . We therefore regard such a model including a timeshift as the appropriate model.

Concerning the RV data a last concern remains. As can be seen from the lower panel in Fig. 6 c) *all* RV data points from the transit night agree within their  $1 \sigma$  uncertainties with the model. This suggests that the uncertainty intervals provided by the DRS<sup>2</sup> pipeline are too conservative. To quantify, there are 6 effective parameters which are (also) controlled by the HARPS-N RVs ( $\Delta T_0$ ,  $\gamma_{\text{HARPS-N}}$ ,  $\lambda$ ,  $v \sin i$ ,  $q_1 + q_2$ ,  $\zeta$ , and  $\xi$ , of which the last four are further constrained by priors and the OOT CCF). There are 42 HARPS-N RV measurements resulting in 36 degrees of freedom. We find a  $\chi^2$  of 10.07 and a reduced  $\chi^2$  of 0.28. This would then suggest that the uncertainty interval we obtain for the projected obliquity from the fit to the RVs might be overestimated. Indeed the interval is about twice the size as for the other two methods. Another indication that the RV confidence interval might be overestimated comes from the comparison to the other two approaches. Given the moderate projected rotation speed of the star the uncertainty intervals between these different methods should not differ by a factor  $\sim 2$  as the shadow and slope methods benefit more with if the host has larger  $v \sin i$ .

In summary we find that our results for  $\lambda$  – using the three different methods on the same data – are consistent with each other ( $\lambda = -2 \pm 15^\circ$ ,  $\lambda = -1 \pm 7^\circ$ ,  $\lambda = 0 \pm 7^\circ$ ) as expected, see Table 2. Given the probably too large uncertainty interval from the fit to the anomalous RVs (probably a result of too conservative RV uncertainties) we use the projected obliquity value as derived from the fit to the shadow as final parameter, meaning  $\lambda = -1 \pm 7^\circ$  is our final value for the projected obliquity.

## 5. Discussion

While finalizing this manuscript we became aware of a recent measurement of the projected obliquity in this system by Sedaghati et al. (2021). They observed HD 332231 during a transit night in October 2020, employing the CARMENES high resolution spectrograph (Quirrenbach et al. 2014) installed at the 3.5m telescope at the Calar Alto Observatory, Spain. This team finds a projected obliquity of  $\lambda = -42.0^{+11.3}_{-10.6}^\circ$ . This value is not in agreement with our final result,  $\lambda = -1 \pm 7^\circ$ . We suspect that there might be at least two reasons for the apparent disagreement of these two measurements. Firstly, that team relied on priors solely derived from the Sector 14 and 15 TESS photometry by Dalba et al. (2020), and their spectroscopic transit observations have been obtained about a year after these TESS observations (about two months after our spectroscopic transit observations). Therefore, their assumption of linear ephemeris might be as erroneous as our initial assumption of linear ephemeris. In fact their result analyzing the anomalous RVs observed during transit is similar to our initial result ( $\lambda = -31 \pm 6^\circ$ ) using the linear ephemeris derived from the TESS photometry.

A second potential reason for the mismatch might be connected to their result for the projected stellar rotation speed. They find  $v \sin i = 16.3^{+6.9}_{-4.4} \text{ km s}^{-1}$ . This is significantly higher than the three values ( $5.3 \pm 1.0 \text{ km s}^{-1}$ ,  $5.4 \pm 1.0 \text{ km s}^{-1}$ , and  $7.0 \pm 0.5 \text{ km s}^{-1}$ ) reported in the discovery paper (Dalba et al. 2020). That value is also difficult to reconcile with the width of the CCFs we have observed, Fig. 4. Therefore, it is also significantly higher than what we find in our overall analysis. As discussed in Albrecht et al. (2011) for low impact transits such as this one a prior on  $v \sin i$  can have significant influence on the derived value for  $\lambda$ .

It would be interesting to see if using a lower  $v \sin i$  value, as well as allowing for a shift in transit mid-time, would not only lead to a consistent result for  $\lambda$ , but also to a similar result for the specific transit mid-time as the spectroscopic transits are only two months apart.

With the data at hand we can not with certainty determine the cause for the departure from linear ephemeris. One possibility would be a second planet which gravitational influence perturbs the orbit of planet b from a purely Keplerian orbit. The presence

<sup>2</sup> The "HIERARCH TNG DRS DVRMS" entry in the FITS header.

and parameters of such a potential third body may be investigated by i) additional RV monitoring to detect long term RV drifts, as well as ii) ground based transit observations to measure TTVs. iii) In August 2022 the system will be observed again in TESS' Sector 55. iv) Additionally, upcoming *Gaia* (Gaia Collaboration et al. 2016) data releases should be able to further clarify the nature of this potential body by detecting or giving upper limits to the reflex motion of the central star caused by such a potential outer body.

Our result for the projected obliquity,  $\lambda = -1 \pm 7^\circ$ , suggests that the obliquity  $\psi$  is low as well and the system is spin-orbit aligned. Given the  $a/R$  of about 24.5 this system might not have been influenced by tides. Therefore, the alignment we are seeing might be primordial. This together with the low eccentricity of the orbit ( $e = 0.030^{+0.017}_{-0.030}$ ), fully consistent with a circular orbit, fits in a picture that orbital inclinations are often associated with high eccentricities as illustrated in Fig. 9. In this picture HD 332231 b has not undergone high eccentricity migration. Dawson & Murray-Clay (2013) noticed that eccentric WJs tend to orbit metal rich rich ( $[\text{Fe}/\text{H}] > 0$ ) hosts while planets on circular orbits tend to be found around stars with lower metallicity. The solar metallicity measured for HD 332231 agrees with this picture.

## 6. Conclusion

We measured the projected obliquity of the bright F8 dwarf HD 332231 using HARPS-N data acquired during transit of the warm giant planet HD 332231 b discovered by Dalba et al. (2020). We use three different approaches to analyze the RM effect. We model the planet shadow, the sub-planetary velocities, and the anomalous in transit RVs. We find fully consistent results. Our measurement of the projected obliquity  $\lambda = -1 \pm 7^\circ$  is consistent with alignment. Since the discovery of the planet, additional TESS photometry from Sector 41 became available and we use it here to further refine the system parameters, specifically the planetary radius and linear ephemeris. We also found an apparent shift of  $\approx 20$  min in the mid-transit time of the transit observed 4th August, 2020 with HARPS-N at the TNG. This shift is relative to the linear ephemeris obtained from transits observed by TESS Summer 2019 and 2021. This shift might be explained by the presence of a third body in the system and future RV, transit, and astrometric observations should be able to find such a body. Our results for the system architecture are consistent with the planet having migrated to its current orbit via disk migration or born in-situ.

**Acknowledgements.** The authors thank Paul Dabla for early discussions on TOI-1456. The authors thank Antonio Magazzu and Rosario Consentino at the TNG as well as Davide Gandolfi for helping with the HARPS-N data. The authors thank Debra Fischer for attempting to observe an ingress of the transit in HD 332231 with the Lowell Discovery Telescope before it was observed with HARPS-N at the TNG. Based on observations (programme ID: A41/TAC19) made with the Italian Telescopio Nazionale Galileo (TNG) operated on the island of La Palma by the Fundación Galileo Galilei of the INAF (Istituto Nazionale di Astrofisica) at the Spanish Observatorio del Roque de los Muchachos of the Instituto de Astrofísica de Canarias. Funding for the Stellar Astrophysics Centre is provided by The Danish National Research Foundation (Grant agreement no.: DNRF106). This paper includes data collected with the TESS mission, obtained from the MAST data archive at the Space Telescope Science Institute (STScI). Funding for the TESS mission is provided by the NASA Explorer Program. STScI is operated by the Association of Universities for Research in Astronomy, Inc., under NASA contract NAS 5–26555. The numerical results presented in this work were obtained at the Centre for Scientific Computing, Aarhus <http://phys.au.dk/forskning/cscaa/>. This research made use of Astropy,<sup>3</sup> a community-developed core Python package for Astronomy (Astropy

Collaboration et al. 2013, 2018). This research made use of matplotlib (Hunter 2007). This research made use of TESScut (Brasseur et al. 2019). This research made use of astropplan (Morris et al. 2018). This research made use of SciPy (Virtanen et al. 2020). This research made use of corner (Foreman-Mackey 2016).

## References

- Albrecht, S., Reffert, S., Snellen, I., Quirrenbach, A., & Mitchell, D. S. 2007, *A&A*, 474, 565
- Albrecht, S., Winn, J. N., Johnson, J. A., et al. 2011, *ApJ*, 738, 50
- Albrecht, S., Winn, J. N., Johnson, J. A., et al. 2012a, *ApJ*, 757, 18
- Albrecht, S., Winn, J. N., Johnson, J. A., et al. 2012b, *ApJ*, 757, 18
- Albrecht, S., Winn, J. N., Marcy, G. W., et al. 2013, *ApJ*, 771, 11
- Andersen, M. F., Grundahl, F., Christensen-Dalsgaard, J., et al. 2014, in *Revista Mexicana de Astronomía y Astrofísica Conference Series*, Vol. 45, *Revista Mexicana de Astronomía y Astrofísica Conference Series*, 83
- Astropy Collaboration, Price-Whelan, A. M., Sipőcz, B. M., et al. 2018, *AJ*, 156, 123
- Astropy Collaboration, Robitaille, T. P., Tollerud, E. J., et al. 2013, *A&A*, 558, A33
- Baruteau, C., Crida, A., Paardekooper, S. J., et al. 2014, in *Protostars and Planets VI*, ed. H. Beuther, R. S. Klessen, C. P. Dullemond, & T. Henning, 667
- Bate, M. R. 2018, *MNRAS*, 475, 5618
- Bate, M. R., Lodato, G., & Pringle, J. E. 2010, *MNRAS*, 401, 1505
- Batygin, K. 2012, *Nature*
- Bonomo, A. S., Desidera, S., Benatti, S., et al. 2017, *A&A*, 602, A107
- Borderies, N., Goldreich, P., & Tremaine, S. 1984, *ApJ*, 284, 429
- Brasseur, C. E., Phillip, C., Fleming, S. W., Mullally, S. E., & White, R. L. 2019, *Astrocute: Tools for creating cutouts of TESS images*
- Brown, D. J. A., Cameron, A. C., Anderson, D. R., et al. 2012, *MNRAS*, 423, 1503
- Cegla, H. M., Lovis, C., Bourrier, V., et al. 2016, *A&A*, 588, A127
- Chatterjee, S., Ford, E. B., Matsumura, S., & Rasio, F. A. 2008, *ApJ*, 686, 580
- Claret, A. 2017, *A&A*, 600, A30
- Claret, A., Hauschildt, P. H., & Witte, S. 2013, *A&A*, 552, A16
- Cosentino, R., Lovis, C., Pepe, F., et al. 2012, in *Society of Photo-Optical Instrumentation Engineers (SPIE) Conference Series*, Vol. 8446, *Ground-based and Airborne Instrumentation for Astronomy IV*, 84461V
- Dalba, P. A., Gupta, A. F., Rodríguez, J. E., et al. 2020, *AJ*, 159, 241
- Dawson, R. I. & Johnson, J. A. 2018, *ARA&A*, 56, 175
- Dawson, R. I. & Murray-Clay, R. A. 2013, *ApJ*, 767, L24
- Doyle, A. P., Davies, G. R., Smalley, B., Chaplin, W. J., & Elsworth, Y. 2014, *MNRAS*, 444, 3592
- Dravins, D., Ludwig, H.-G., Dahlén, E., & Pazira, H. 2017, *A&A*, 605, A90
- Fabrycky, D. & Tremaine, S. 2007, *ApJ*, 669, 1298
- Fielding, D. B., McKee, C. F., Socrates, A., Cunningham, A. J., & Klein, R. I. 2015, *MNRAS*, 450, 3306
- Foreman-Mackey, D. 2016, *The Journal of Open Source Software*, 1, 24
- Foreman-Mackey, D., Hogg, D. W., Lang, D., & Goodman, J. 2013, *PASP*, 125, 306
- Foucart, F. & Lai, D. 2011, *MNRAS*, 412, 2799
- Gaia Collaboration, Brown, A. G. A., Vallenari, A., et al. 2018, *A&A*, 616, A1
- Gaia Collaboration, Prusti, T., de Bruijne, J. H. J., et al. 2016, *A&A*, 595, A1
- Gratia, P. & Fabrycky, D. 2017, *MNRAS*, 464, 1709
- Gray, D. F. 2005, *The Observation and Analysis of Stellar Photospheres*, 3<sup>rd</sup> Ed. (ISBN 0521851866, Cambridge University Press)
- Grundahl, F., Fredslund Andersen, M., Christensen-Dalsgaard, J., et al. 2017, *ApJ*, 836, 142
- Guerrero, N. M., Seager, S., Huang, C. X., et al. 2021, *ApJS*, 254, 39
- Hirano, T., Suto, Y., Winn, J. N., et al. 2011, *ApJ*, 742, 69
- Hjorth, M., Albrecht, S., Hirano, T., et al. 2021, *Proceedings of the National Academy of Science*, 118, 2017418118
- Hoeijmakers, H. J., Cabot, S. H. C., Zhao, L., et al. 2020, *A&A*, 641, A120
- Høg, E., Fabricius, C., Makarov, V. V., et al. 2000, *A&A*, 355, L27
- Huber, D., Carter, J. A., Barbieri, M., et al. 2013, *Science*, 342, 331
- Hunter, J. D. 2007, *Computing in Science & Engineering*, 9, 90
- Husnoo, N., Pont, F., Mazeh, T., et al. 2012, *MNRAS*, 422, 3151
- Jenkins, J. M., Twicken, J. D., McCaulliff, S., et al. 2016, in *Society of Photo-Optical Instrumentation Engineers (SPIE) Conference Series*, Vol. 9913, *Software and Cyberinfrastructure for Astronomy IV*, ed. G. Chiozzi & J. C. Goodman, 99133E
- Johnson, M. C., Cochran, W. D., Albrecht, S., et al. 2014, *ApJ*, 790, 30
- Kreidberg, L. 2015, *PASP*, 127, 1161
- Kumar, R., Carroll, C., Hartikainen, A., & Martin, O. 2019, *Journal of Open Source Software*, 4, 1143
- Lai, D., Foucart, F., & Lin, D. N. C. 2011, *MNRAS*, 412, 2790
- Laskar, J. 2008, *Icarus*, 196, 1

<sup>3</sup> <http://www.astropy.org>

- Lightkurve Collaboration, Cardoso, J. V. d. M., Hedges, C., et al. 2018, Lightkurve: Kepler and TESS time series analysis in Python, Astrophysics Source Code Library
- Lin, D. N. C., Bodenheimer, P., & Richardson, D. C. 1996, *Nature*, 380, 606
- Lubow, S. H. & Ogilvie, G. I. 2000, *ApJ*, 538, 326
- Mandel, K. & Agol, E. 2002, *ApJ*, 580, L171
- Matsakos, T. & Königl, A. 2017, *AJ*, 153, 60
- Mayor, M., Pepe, F., Queloz, D., et al. 2003, *The Messenger*, 114, 20
- McLaughlin, D. B. 1924, *ApJ*, 60, 22
- Morris, B. M., Tollerud, E., Sipocz, B., et al. 2018, *astroplan*: Observation planning package for astronomers
- Nagasawa, M., Ida, S., & Bessho, T. 2008, *ApJ*, 678, 498
- Naoz, S. 2016, *ARA&A*, 54, 441
- Quirrenbach, A., Amado, P. J., Caballero, J. A., et al. 2014, in *Society of Photo-Optical Instrumentation Engineers (SPIE) Conference Series*, Vol. 9147, *Ground-based and Airborne Instrumentation for Astronomy V*, ed. S. K. Ramsay, I. S. McLean, & H. Takami, 91471F
- Radovan, M. V., Cabak, G. F., Laiterman, L. H., Lockwood, C. T., & Vogt, S. S. 2010, in *Society of Photo-Optical Instrumentation Engineers (SPIE) Conference Series*, Vol. 7735, *Ground-based and Airborne Instrumentation for Astronomy III*, ed. I. S. McLean, S. K. Ramsay, & H. Takami, 77354K
- Radovan, M. V., Lenclos, K., Holden, B. P., et al. 2014, in *Society of Photo-Optical Instrumentation Engineers (SPIE) Conference Series*, Vol. 9145, *Ground-based and Airborne Telescopes V*, ed. L. M. Stepp, R. Gilmozzi, & H. J. Hall, 91452B
- Ricker, G. R., Winn, J. N., Vanderspek, R., et al. 2015, *Journal of Astronomical Telescopes, Instruments, and Systems*, 1, 014003
- Romanova, M. M., Koldoba, A. V., Ustyugova, G. V., et al. 2021, *MNRAS*[arXiv:2012.10826]
- Rossiter, R. A. 1924, *ApJ*, 60, 15
- Savitzky, A. & Golay, M. J. E. 1964, *Analytical Chemistry*, 36, 1627
- Sedaghati, E., Sánchez-López, A., Czesla, S., et al. 2021, *arXiv e-prints*, arXiv:2110.10282
- Shporer, A. & Brown, T. 2011, *ApJ*, 733, 30
- Spalding, C., Batygin, K., & Adams, F. C. 2014, *ApJ*, 797, L29
- Struve, O. & Elvey, C. T. 1931, *MNRAS*, 91, 663
- Takaishi, D., Tsukamoto, Y., & Suto, Y. 2020, *arXiv e-prints*, arXiv:2001.05456
- Teyssandier, J., Lai, D., & Vick, M. 2019, *MNRAS*, 486, 2265
- Thies, I., Kroupa, P., Goodwin, S. P., Stamatellos, D., & Whitworth, A. P. 2011, *MNRAS*, 417, 1817
- Vehtari, A., Gelman, A., Simpson, D., Carpenter, B., & Bürkner, P.-C. 2019, *arXiv e-prints*, arXiv:1903.08008
- Virtanen, P., Gommers, R., Oliphant, T. E., et al. 2020, *Nature Methods*, 17, 261
- Vogt, S. S., Allen, S. L., Bigelow, B. C., et al. 1994, in *Society of Photo-Optical Instrumentation Engineers (SPIE) Conference Series*, Vol. 2198, *Instrumentation in Astronomy VIII*, ed. D. L. Crawford & E. R. Craine, 362
- Vogt, S. S., Radovan, M., Kibrick, R., et al. 2014, *PASP*, 126, 359
- Winn, J. N., Fabrycky, D., Albrecht, S., & Johnson, J. A. 2010, *ApJ*, 718, L145
- Wu, Y. & Lithwick, Y. 2011, *ApJ*, 735, 109
- Wu, Y. & Murray, N. 2003, *ApJ*, 589, 605
- Zanazzi, J. J. & Lai, D. 2018, *MNRAS*, 478, 835
- Zhou, G., Latham, D. W., Bieryla, A., et al. 2016, *MNRAS*, 460, 3376

**Table A.1.** RVs and subplanetary velocities determined from our HARPS-N data. The epoch refers to the flux weighted midpoint of the observations. From the RVs listed here we have subtracted the systemic velocity,  $\gamma_{\text{HARPS-N}}$ , from our MCMC using the RVs (Table 2).

| Epoch<br>BTJD <sub>TDB</sub> | RV- $\gamma_{\text{HARPS-N}}$ , RV<br>m s <sup>-1</sup> | $v_p$<br>km s <sup>-1</sup> |
|------------------------------|---|-----------------------------|
| 2066.389858                  | 9.1 ± 4.0   | -4.9 ± 2.6                  |
| 2066.396375                  | 11.1 ± 4.0  | -5.3 ± 1.7                  |
| 2066.402856                  | 20.5 ± 3.7  | -5.1 ± 1.3                  |
| 2066.409604                  | 20.0 ± 3.9  | -5.7 ± 1.0                  |
| 2066.416248                  | 23.0 ± 4.0  | -4.8 ± 0.8                  |
| 2066.422834                  | 25.9 ± 3.8  | -4.8 ± 0.5                  |
| 2066.429211                  | 23.7 ± 4.1  | -4.1 ± 0.6                  |
| 2066.435565                  | 23.2 ± 4.0  | -3.7 ± 0.6                  |
| 2066.442417                  | 23.1 ± 4.5  | -3.4 ± 0.6                  |
| 2066.449038                  | 23.8 ± 4.1  | -3.0 ± 0.6                  |
| 2066.455485                  | 22.1 ± 4.1  | -2.8 ± 0.7                  |
| 2066.462047                  | 19.0 ± 4.2  | -2.5 ± 0.6                  |
| 2066.468506                  | 17.4 ± 4.7  | -2.5 ± 0.8                  |
| 2066.474999                  | 19.9 ± 4.8  | -2.1 ± 0.7                  |
| 2066.481608                  | 15.7 ± 4.6  | -1.8 ± 0.8                  |
| 2066.488055                  | 13.2 ± 4.6  | -1.2 ± 0.6                  |
| 2066.494652                  | 8.6 ± 4.9   | -0.4 ± 0.6                  |
| 2066.501215                  | 8.0 ± 5.5   | -0.4 ± 0.7                  |
| 2066.508125                  | 4.5 ± 5.3   | -0.1 ± 1.0                  |
| 2066.514525                  | 2.8 ± 5.4   | -0.0 ± 0.7                  |
| 2066.521007                  | -4.8 ± 5.2  | 1.0 ± 0.6                   |
| 2066.527465                  | -5.5 ± 5.1  | 0.8 ± 0.5                   |
| 2066.534144                  | -5.4 ± 5.2  | 0.8 ± 0.7                   |
| 2066.540255                  | -11.4 ± 5.6   | 1.4 ± 0.5                   |
| 2066.547223                  | -12.1 ± 5.3   | 2.1 ± 0.7                   |
| 2066.553658                  | -14.6 ± 5.2   | 2.0 ± 0.8                   |
| 2066.560221                  | -14.5 ± 5.7   | 2.8 ± 0.9                   |
| 2066.566876                  | -14.9 ± 5.8   | 3.0 ± 0.9                   |
| 2066.573276                  | -14.9 ± 5.6   | 3.4 ± 1.1                   |
| 2066.579735                  | -18.0 ± 5.6   | 3.3 ± 0.8                   |
| 2066.586494                  | -23.1 ± 5.0   | 3.9 ± 0.7                   |
| 2066.592895                  | -23.4 ± 5.7   | 3.5 ± 1.0                   |
| 2066.599550                  | -21.4 ± 5.7   | 5.1 ± 1.2                   |
| 2066.606078                  | -16.4 ± 5.6   | 5.0 ± 1.4                   |
| 2066.612305                  | -21.3 ± 5.8   | 5.3 ± 0.9                   |
| 2066.619215                  | -14.9 ± 5.7   | 4.5 ± 1.6                   |
| 2066.625696                  | -9.0 ± 5.9  | 4.3 ± 2.6                   |
| 2066.631854                  | -1.3 ± 5.6  | 5.0 ± 1.0                   |
| 2066.638544                  | -4.8 ± 5.8  | 2.5 ± 5.2                   |
| 2066.645430                  | 3.3 ± 5.2   | -                           |
| 2066.652039                  | -4.1 ± 4.5  | -                           |
| 2066.658498                  | 0.3 ± 4.5   | -                           |

## Appendix A: Table of radial and subplanetary velocities